LETTER

doi:10.1038/nature13382

Visualizing the kinetic power stroke that drives proton–coupled zinc(II) transport

Sayan Gupta[1]†, Jin Chai[2], Jie Cheng[3], Rhijuta D'Mello[1], Mark R. Chance[1] & Dax Fu[2,3]

The proton gradient is a principal energy source for respiration-dependent active transport, but the structural mechanisms of proton-coupled transport processes are poorly understood. YiiP is a proton-coupled zinc transporter found in the cytoplasmic membrane of *Escherichia coli*. Its transport site receives protons from water molecules that gain access to its hydrophobic environment and transduces the energy of an inward proton gradient to drive Zn(II) efflux[1,2]. This membrane protein is a well-characterized member[3–7] of the family of cation diffusion facilitators that occurs at all phylogenetic levels[8–10]. Here we show, using X-ray-mediated hydroxyl radical labelling of YiiP and mass spectrometry, that Zn(II) binding triggers a highly localized, all-or-nothing change of water accessibility to the transport site and an adjacent hydrophobic gate. Millisecond time-resolved dynamics reveal a concerted and reciprocal pattern of accessibility changes along a transmembrane helix, suggesting a rigid-body helical re-orientation linked to Zn(II) binding that triggers the closing of the hydrophobic gate. The gated water access to the transport site enables a stationary proton gradient to facilitate the conversion of zinc-binding energy to the kinetic power stroke of a vectorial zinc transport. The kinetic details provide energetic insights into a proton-coupled active-transport reaction.

Mammalian homologues of YiiP are responsible for zinc sequestration into secretory vesicles, thus playing important roles in neurotransmission[11] and hormone secretion[12]. Zinc efflux catalysed by YiiP is coupled with proton influx in a 1:1 zinc-for-proton exchange stoichiometry[3]. When protons are scarce at higher pH, zinc transport comes to a halt despite a large zinc concentration gradient[7]. Thus, the zinc-for-proton coupling is obligatory. Biochemical studies and X-ray structures of YiiP showed that zinc transport is mediated by a tetrahedral Zn(II)-binding site in the centre of the transmembrane domain (TMD)[1,4]. This intramembranous zinc-transport site adopts coordination geometry satisfied by three Asp and one His residues, but lacks any additional polar or charged residues in the Zn(II)-binding pocket. The absence of available pH titratable residues in the second coordination sphere necessitates water access to fulfil proton donor or acceptor functions to enable the obligatory zinc-for-proton exchange. However, the crystal structure of zinc-bound YiiP (zinc-YiiP) shows that water access to the transport site is blocked by hydrophobic residues that divide the zinc translocation pathway into an extracellular and intracellular cavity[13]. A protein conformational change is expected to open up a water portal within the hydrophobic seal. As water molecules gain access to the transport site in a transport reaction cycle, irradiating YiiP to a millisecond synchrotron X-ray pulse could render residues in contact with waters susceptible to hydroxyl-radical-mediated oxidative modification, thereby permitting the monitoring of residues motions in terms of water accessibility change[14,15]. Radiolytic hydroxyl radicals under such experimental conditions are generated rapidly and isotropically both in bulk and activated bound waters with side-chain oxidation completed within milliseconds[15–18]. By comparison, the macroscopic timescale for zinc transport is of the order of 200–500 ms[3,7]. Thus, time-resolved hydroxyl radical 'footprinting' would have a sufficient time resolution to monitor proton translocation and associated protein conformational change.

Purified YiiP in detergent micelles was exposed to a focused synchrotron white beam, followed by a rapid mix with methionine-amide to quench secondary radical chain reactions (Extended Data Fig. 1a). The effective hydroxyl radical concentration was controlled in the micromolar range as indicated by an Alexa Fluor 488 dosimeter, and secondary radiation damage of YiiP was minimized by adjusting the X-ray irradiation to an optimal dose range[14,16]. As a result, only negligible differences in size-exclusion high-performance liquid chromatography (HPLC) profiles were observed for the protein peaks before and after X-ray irradiation (Fig. 1a). The broad low molecular peak in zinc-YiiP (red trace) corresponded to the methionine-amide quencher added to the apo-YiiP sample after irradiation. The sites of oxidative modification were characterized by +14, +16 and +32 dalton (Da) oxygen-based mass adducts[14,15,18], which were detected by bottom-up liquid chromatography–mass spectrometry (LC–MS) of proteolytic fragments of the irradiated YiiP (Fig. 1b), and confirmed by tandem mass spectrometry (MS/MS) assignments (Fig. 1c). The overall mass spectrometric sequence coverage was 82% (Extended Data Fig. 2a), encompassing all residues located within the inter-cavity seal (Extended Data Fig. 2b). Increasing X-ray irradiation progressively increased the modified and reduced the unmodified populations, giving rise to a dose–response plot for each modified site (Fig. 1d and Extended Data Fig. 3). The initial phase of the dose–response plot followed a pseudo-first-order reaction, but occasional deviations from the exponential function were observed at increased irradiation times as a result of secondary modifications (Fig. 1d and Extended Data Fig. 3). Therefore, the slope of the initial phase was used to quantify the hydroxyl radical reactivity (Extended Data Table 1).

The rate of side-chain labelling is governed by intrinsic reactivity of the amino acid and water accessibility to the side chain[14,15]. The ratio of the measured reactivity rates for the same residue from zinc-YiiP and apo-YiiP gave a ratiometric account of the water accessibility change independent of the intrinsic side-chain reactivity or sequence context. Among all the detectable sites of modification, two sites exhibited conspicuously large differences in reactivity in the presence and absence of zinc (Fig. 2a). One instance where Zn(II) binding reduced reactivity more than 1000-fold was observed for three consecutive residues, V48, D49 and I50, within the peptide LVDI of TM2 (Extended Data Table 1). In the crystal structure of zinc-YiiP (Protein Data Bank accession number 3H90), D49 binds Zn(II) in the transport site and is one helical turn away from a structural water that is immobilized via a hydrogen bond to S53 (3.1 Å to Oγ) (Fig. 3a). Coordination of Zn(II) to the transport site may suppress productive radiolysis of this structural water, resulting in a negligible rate of VDI labelling in zinc-YiiP (Extended Data Table 1). In sharp contrast, the absence of a coordinated Zn(II) in apo-YiiP permitted an unusually fast radiolytic labelling at 163 s^{-1} (Extended Data Table 1). Such a high level of reactivity has been observed for radiolytic labelling by structural water molecules in the hydrophobic core of a G-protein-coupled receptor[17].

A second very significant change was observed for a +14 Da modification of L152 in the peptide ADMLHY of TM5 (Fig. 2a). In apo-YiiP, the rate of +14 Da modification for L152 was 8.5 s^{-1} (Extended Data Table 1) while Zn(II) binding reduced the reactivity of L152 more than 100-fold, to a negligible level, illustrating that a Zn(II)-binding-induced conformational

[1]Center for Synchrotron Biosciences and Center for Proteomics and Bioinformatics, Case Western Reserve University, Cleveland, Ohio 44109, USA. [2]Biology Department, Brookhaven National Laboratory, Upton, New York 11973, USA. [3]Department of Physiology, Johns Hopkins School of Medicine, Baltimore, Maryland 21205, USA. †Present address: Berkeley Center for Structural Biology, Physical Biosciences Division, Lawrence Berkeley National Laboratory, Berkeley, California 94720, USA.

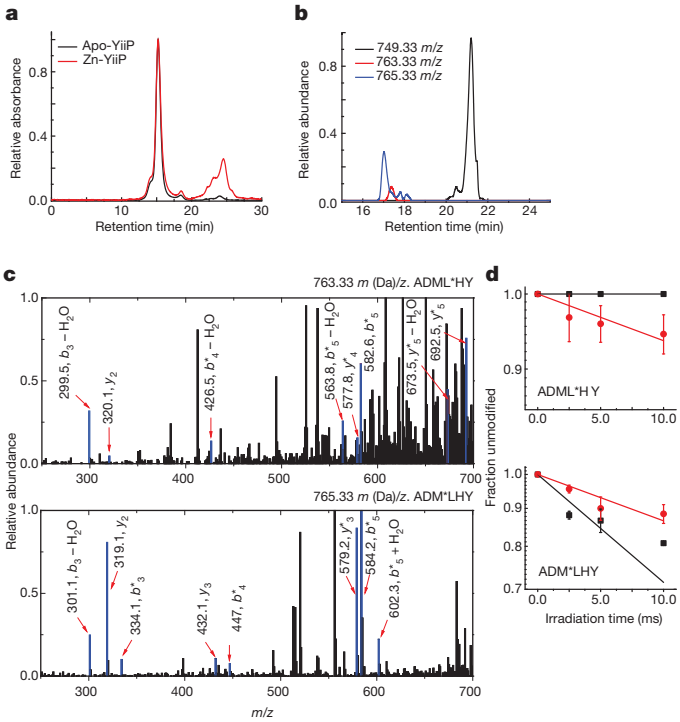

Figure 1 | Radiolytic labelling and mass spectrometric analysis. **a**, Size-exclusion HPLC chromatograms of apo-YiiP before irradiation and zinc-YiiP after irradiation. **b**, Examples for quantification of radiolytic labelling by LC–MS; extracted ion-count chromatograms of singly protonated, unmodified (749.33 *m*/*z*, black), carbonylated (+14 Da mass shift, 763.33 *m*/*z*, red) and hydroxylated (+16 Da mass sift, 765.33 *m*/*z*, blue) peptide ADMLHY. **c**, Examples for identification of modified residues by MS/MS of the carbonylated and hydroxylated ADMLHY with peak assignments (red arrow and blue line) confirming L152 and M151 modification, respectively. **d**, Dose–responses showing reciprocal solvent accessibility changes at L152 and M151 sites in apo-YiiP (red) and zinc-YiiP (black). Solid lines, least-squares fits of the means of dose-dependent data; error bar, s.e.m. from four to six independent measurements.

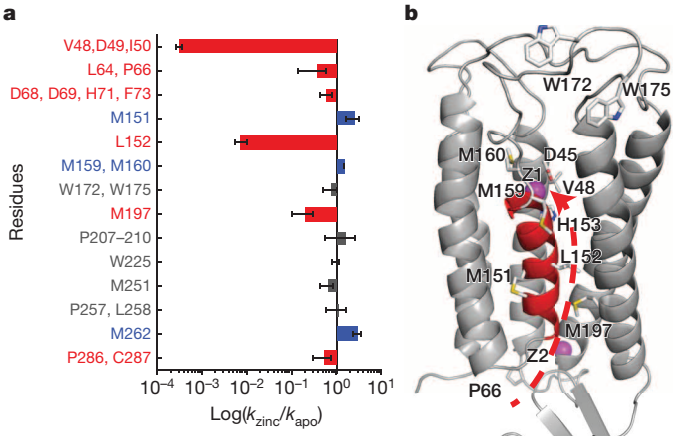

Figure 2 | Quantification of water accessibility changes. **a**, Water accessibility changes in response to Zn(II) binding measured by the ratio of labelling rates for residues with an increase (blue), decrease (red) or no change (grey) in water accessibility after a rapid Zn(II) exposure. The labelling rate for each site as indicated is summarized in Extended Data Table 1, and the error bar represents the standard error from four to six independent measurements. **b**, Residues with a partial water accessibility change in response to zinc binding. TM5 is coloured in red. Z1 and Z2 (magenta spheres) represent bound zinc ions. Arrow indicates a putative zinc-transport pathway from the cytoplasm through the L152 gate to the transport site.

change removed water access to the side chain of L152. This peptide contained another labelled residue, M151, whose +16 Da modified products could be isolated from those of L152 on the basis of the difference in the mass to charge ratio (*m*/*z*) (Fig. 1b, c). The same conformational change that reduced reactivity of L152 yielded a 2.5-fold increase in reactivity for the neighbouring M151 (Figs 1d and 2a). In the zinc-YiiP structure, L152 is fully buried and oriented towards the intracellular cavity as a part of the inter-cavity seal, consistent with the lack of radiolytic labelling (Fig. 3a).

L152 is located at the interface between a TM3–TM6 helix pair and a compact TM1–TM2–TM4–TM5 four-helix bundle (Fig. 3b). These two subdomains cross over to form two cavities located on either side of the membrane as indicated by arrows in Fig. 3b. The inter-domain packing wedges TM5 (coloured in red) at one corner of the four-helix bundle into the TM3–TM6 interface with L152 situated at the centre of the TM5→TM3–TM6 triple-helix joint (Fig. 3b). L152 interacts with I90 from TM3 and A194 from TM6 to form a tight knob-into-hole packing. The I90 equivalents have been identified as metal determinant residues in plant and yeast cation diffusion facilitator (CDF) homologues[19,20]. One helical turn down towards the intracellular cavity is another layer of residue triad: A83 from TM3, A149 from TM5 and M197 from TM6, which define the innermost section of the intracellular cavity (Fig. 3b). Of note, the conformational changes of M197 echo those of L152, with a zinc-dependent reduction of solvent accessibility (Fig. 2a) except that the accessibility of M197 is not reduced to the background level in the zinc-bound state (Extended Data Fig. 3). This cluster of six residues forms a highly conserved TM5→TM3–TM6 packing core (Extended Data Fig. 4), with L152 serving as a principal hydrophobic barrier between the two cavities (Fig. 3c, d). The structural and functional importance of L152 was examined by a series of point mutations (Extended Data Fig. 5). All L152 mutants expressed well. However, substitutions of L152 with smaller (G, A), bulky aromatic (F) and charged residues (D, R) resulted in complete denaturation after the mutant proteins were solubilized by DDM, whereas conserved L152 substitutions with I and M residues were partly tolerated

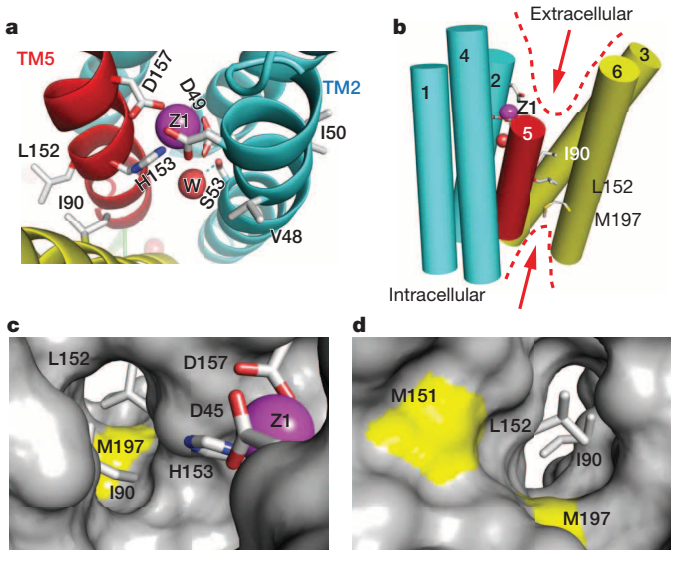

Figure 3 | L152 controls the opening of an inter-cavity water portal. **a**, A structural water molecule (W, red sphere) near the transport site occupied by a tetrahedral coordinated Zn(II) (Z1, magenta sphere), viewed from the periplasm. Relevant residues are drawn in sticks and labelled accordingly. TM5 is coloured in red as indicated. **b**, Intracellular and extracellular cavity as outlined by dashed lines. **c**, L152 gate viewed from the extracellular cavity along the arrow as indicated in **b**. The side chains of L152, I90 and the coordination residues in the transport site (sticks) are excluded from the protein surface drawing. M197 is shown as a yellow patch at the cytoplasmic entrance to the inter-cavity portal. **d**, L152 gate viewed from the intracellular cavity along the arrow as indicated in **b**. M151 and M197 are visible as yellow patches on the protein surface.

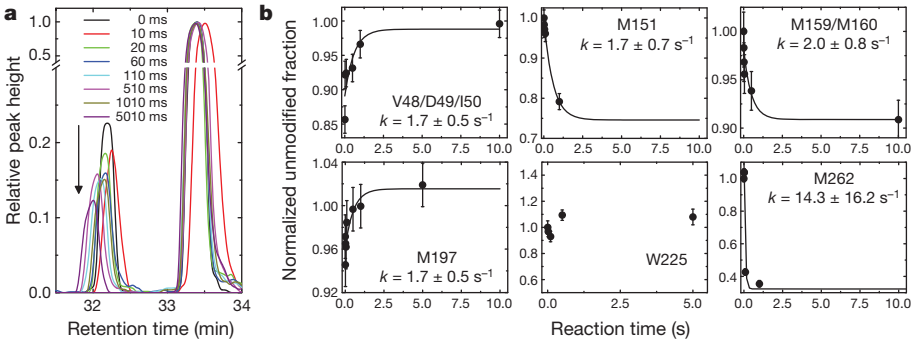

Figure 4 | Kinetics of water accessibility changes. **a**, An example of extracted ion chromatograms from the unmodified and modified M197 in peptide 197–208. The data were smoothed by a low-pass filter and normalized to the peak height of respective unmodified species. The arrow indicates a progressive decrease of the modified peaks as a function of the reaction time. **b**, Time courses of water accessibility change for indicated residues. The solid line represents a single exponential fit of the time course of the unmodified fraction with a fitted rate constant (k) presented as mean ± s.e.m. from six independent measurements.

(Extended Data Fig. 5). The side-chain-dependent effects of L152 mutations on protein stability are consistent with a critical structural role for L152 in the highly conserved TM5⟶TM3–TM6 packing core.

Among all the detectable sites, only the transport site and its neighbouring L152 gate exhibited all-or-nothing water accessibility changes (Figs 1d and 2a and Extended Data Fig. 3), suggesting a tight control of water leakage across the membrane. Within the TMD, oxidative modifications were observed at four reactive Met residues outside the transport site and the L152 gate. As noted above, M197 at the intracellular entrance to the L152 gate (Fig. 2b) showed a 70% reduction in water accessibility upon Zn(II) binding (Fig. 2a) whereas M151, M159 and M160 at the amino (N) and carboxy (C) termini of TM5 (Fig. 2b) showed a 50–130% increase in water accessibility (Fig. 2a and Extended Data Table 1). These last three Met residues reside on a helical face of TM5 with increased water accessibility upon Zn(II) binding (Fig. 2b). By contrast, residues with a reduction of water accessibility upon Zn(II) binding are either located on the opposite TM5 face (for example, L152) or packed against the opposite TM5 face (V48 and M197) (Fig. 2b). The tetrahedral transport site (H153, D157, D45 and D49) is also located on the same TM5 face with a zinc-dependent loss of water accessibility. The reciprocal change in water accessibility on two opposite TM5 faces is consistent with re-orientation of TM5 in response to Zn(II) binding. Furthermore, solvent-accessible residues in apo-YiiP were found to line a putative transmembrane zinc pathway, starting from M197 in the intracellular cavity, through L152 within the inter-cavity seal and arriving at H153, V48 and D49 in the extracellular cavity (Fig. 2b). This finding of a well-defined channel from the transport site in apo-YiiP to the intracellular cavity is in agreement with an inward-facing conformation revealed by an electron crystallographic structure of an apo-YiiP homologue[21].

To understand the structural dynamics of the Zn-dependent closing of the inter-cavity portal, we monitored the time course of radiolytic modification upon rapid mixing of apo-YiiP and 0.2 mM $ZnCl_2$ (Extended Data Fig. 1b). Only highly reactive residues could be detected with a sufficient signal-to-noise ratio for quantitative kinetic analysis (Fig. 4a). In the TMD, time-resolved measurements were performed on four Met residues (M151, M159/M160 and M197) and the V48/D49/I50 peptide. After mixing of apo-YiiP and Zn(II), the exponential increases in unmodified V48/D49/I50 and M197 residues, indicative of the closing of the inter-cavity portal, mirrored the exponential falls in unmodified M151 and M159/M160 residues (Fig. 4b). The rates of reciprocal water accessibility changes for these four positions on opposite faces of TM5 were identical within experimental errors, suggesting that TM5 underwent a rigid-body re-orientation upon zinc binding. The rigid-body motion of TM5 predicted a similar rate of L152 motion. Averaging the rates of four detectable sites gave an overall rate of TM5 motion at $1.8 \pm 0.7\ s^{-1}$, approximating the macroscopic transport rate ($2–5\ s^{-1}$) determined by stopped-flow Zn(II) flux measurements[3,7]. Thus, zinc access to the transport site and the ensuing TM5 motion linked to the closing of the L152 gate occur on the same time scale. As an internal control, time-resolved measurement showed no changes in labelling to W225 on the cytoplasmic domain (CTD) surface (Fig. 4b). However, another surface residue, M262, exhibited a rapid change at $14.3\ s^{-1}$ (Fig. 4b). The marked kinetic difference suggested that the observed water accessibility change to M262 preceded TM5 motion, but its functional relevance is unclear.

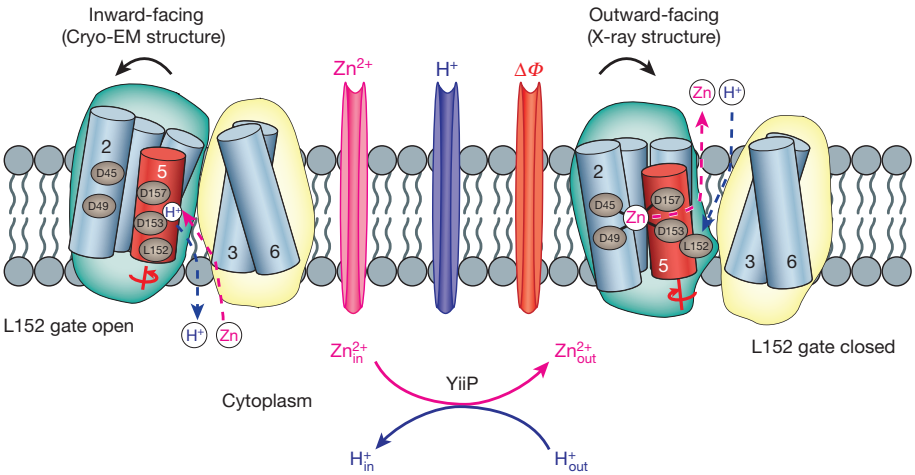

Figure 5 | Schematic representation of zinc-for-proton exchange. The representation is based on two existing structural models with the L152 gate open or closed as indicated. The protein conformational change alternates the membrane-facing on–off mode of zinc coordination and protonation–deprotonation of the transport site in a coordinated fashion.

The time-resolved data suggested that Zn(II) binding triggers a concerted rigid-body motion of TM5 that swings L152 into place to plug the inter-cavity seal (Fig. 5). Since the four coordination residues of the transport site are projected from TM2 and TM5 (Fig. 3a), a TM5 motion is expected to alter the TM2–TM5 inter-helix orientation that determines the coordination geometry of the transport site[1]. Thus, a rigid-body TM5 motion would simultaneously affect the mode of Zn(II) coordination and the gating of the inter-cavity portal through L152 movement (Fig. 5). As shown in Fig. 3c, d, the opening of the L152 gate would expose the transport site through a nanotube to the aqueous bulk of the intracellular cavity[22]. When a Zn(II) from the intracellular cavity reaches the transport site, the favourable match of its coordination chemistry with the tetrahedral transport site[23] would release binding free energy in the confinement of the hydrophobic core where the free energy may be guided to trigger TM5 re-orientation. By analogy to the working of a combustion engine, the released zinc-binding energy is transformed to useful mechanical energy, providing the power stroke of TM5 re-orientation to close the L152 gate (Fig. 5). As a result, this conformational change alternatively exposes the transport site to intracellular and extracellular cavity. The *in vivo* transmembrane proton gradient of an enteric bacterium *E. coli* is about one to two pH units[24]. The flipping of H153 as a part of the transport site to either side of the membrane with a physiological pH gradient is expected to change its protonation state. A deprotonated H153 facing a relatively alkaline cytosol would promote Zn(II) binding from the intracellular cavity whereas a protonated H153 facing a relatively acidic periplasm may facilitate Zn(II) release into the extracellular cavity (Fig. 5). As such, an inward pH gradient drives a vectorial Zn(II) efflux in a 1:1 exchange stoichiometry. The dynamic details revealed in the present study explain how a physiological proton gradient, zinc coordination chemistry and water nanofluidics are orchestrated in a dynamic protein structure to overcome the activation barrier to Zn(II) efflux and promote a vectorial Zn(II) movement through an inter-cavity water portal that is highly conserved in the CDF protein family.

METHODS SUMMARY

YiiP was overexpressed and purified as described previously[3]. Prior to X-ray irradiation, YiiP was de-metallized and then exchanged to a radiolytic labelling buffer (10 mM NaPi, pH 6.5, 100 mM NaCl, 0.02% DDM, 0.1 mM TCEP) by size-exclusion HPLC. $ZnCl_2$ was added to 0.1 mM to an aliquot of apo-YiiP to form zinc-YiiP. Apo-YiiP or zinc-YiiP at a concentration of 10 μM were exposed to an X-ray white beam at 4 °C at beamline X28C of the National Synchrotron Light Source, Brookhaven National Laboratory, as described previously[16,25]. Proteolytic cleavage of the irradiated samples used pepsin, trypsin or trypsin–chymotrypsin double digestion. A bottom-up proteomic analysis by reverse phase liquid chromatography interfaced to a Fourier transform mass spectrometer. The MS/MS data for peptides and their sites of modifications were manually interpreted with the aid of proteomics software[26]. The peak area from the extracted ion chromatograms of a specific peptide fragment was used to quantify the amount of modification. The extent of modification versus the X-ray irradiation time was fitted to a single exponential function to determine the hydroxyl radical reactivity rate of the side chain. Time-resolved radiolysis was performed with a modified KinTek apparatus using a standard flow sequence[18,27]. Apo-YiiP at a concentration of 20 μM, and an equal volume of 0.2 mM $ZnCl_2$ were mixed by a T-mixer. After a designated delay time, the mixed sample was driven through an irradiation cell and then into a quenching tube. The extent of radiolytic modification was plotted against the reaction time and fitted with a single exponential function to determine the rate of water accessibility change. All data are presented as mean ± s.e.m. based on three or more independent measurements.

Online Content Methods, along with any additional Extended Data display items and Source Data, are available in the online version of the paper; references unique to these sections appear only in the online paper.

Received 17 October 2013; accepted 14 April 2014.
Published online 22 June 2014.

1. Lu, M., Chai, J. & Fu, D. Structural basis for autoregulation of the zinc transporter YiiP. *Nature Struct. Mol. Biol.* **16,** 1063–1067 (2009).
2. Grass, G. *et al.* FieF (YiiP) from *Escherichia coli* mediates decreased cellular accumulation of iron and relieves iron stress. *Arch. Microbiol.* **183,** 9–18 (2005).
3. Chao, Y. & Fu, D. Thermodynamic studies of the mechanism of metal binding to the *Escherichia coli* zinc transporter YiiP. *J. Biol. Chem.* **279,** 17173–17180 (2004).
4. Wei, Y. & Fu, D. Selective metal binding to a membrane-embedded aspartate in the *Escherichia coli* metal transporter YiiP (FieF). *J. Biol. Chem.* **280,** 33716–33724 (2005).
5. Wei, Y. & Fu, D. Binding and transport of metal ions at the dimer interface of the *Escherichia coli* metal transporter YiiP. *J. Biol. Chem.* **281,** 23492–23502 (2006).
6. Wei, Y., Li, H. & Fu, D. Oligomeric state of the *Escherichia coli* metal transporter YiiP. *J. Biol. Chem.* **279,** 39251–39259 (2004).
7. Chao, Y. & Fu, D. Kinetic study of the antiport mechanism of an *Escherichia coli* zinc transporter, ZitB. *J. Biol. Chem.* **279,** 12043–12050 (2004).
8. Kambe, T., Yamaguchi-Iwai, Y., Sasaki, R. & Nagao, M. Overview of mammalian zinc transporters. *Cell. Mol. Life Sci.* **61,** 49–68 (2004).
9. Montanini, B., Blaudez, D., Jeandroz, S., Sanders, D. & Chalot, M. Phylogenetic and functional analysis of the cation diffusion facilitator (CDF) family: improved signature and prediction of substrate specificity. *BMC Genomics* **8,** 107 (2007).
10. Nies, D. H. Efflux-mediated heavy metal resistance in prokaryotes. *FEMS Microbiol. Rev.* **27,** 313–339 (2003).
11. Palmiter, R. D., Cole, T. B., Quaife, C. J. & Findley, S. D. ZnT-3, a putative transporter of zinc into synaptic vesicles. *Proc. Natl Acad. Sci. USA* **93,** 14934–14939 (1996).
12. Lemaire, K. *et al.* Insulin crystallization depends on zinc transporter ZnT8 expression, but is not required for normal glucose homeostasis in mice. *Proc. Natl Acad. Sci. USA* **106,** 14872–14877 (2009).
13. Lu, M. & Fu, D. Structure of the zinc transporter YiiP. *Science* **317,** 1746–1748 (2007).
14. Xu, G. & Chance, M. R. Hydroxyl radical-mediated modification of proteins as probes for structural proteomics. *Chem. Rev.* **107,** 3514–3543 (2007).
15. Takamoto, K. & Chance, M. R. Radiolytic protein footprinting with mass spectrometry to probe the structure of macromolecular complexes. *Annu. Rev. Biophys. Biomol. Struct.* **35,** 251–276 (2006).
16. Gupta, S. *et al.* Conformational changes during the gating of a potassium channel revealed by structural mass spectrometry. *Structure* **18,** 839–846 (2010).
17. Angel, T. E., Gupta, S., Jastrzebska, B., Palczewski, K. & Chance, M. R. Structural waters define a functional channel mediating activation of the GPCR, rhodopsin. *Proc. Natl Acad. Sci. USA* **106,** 14367–14372 (2009).
18. Gupta, S., D'Mello, R. & Chance, M. R. Structure and dynamics of protein waters revealed by radiolysis and mass spectrometry. *Proc. Natl Acad. Sci. USA* **109,** 14882–14887 (2012).
19. Podar, D. *et al.* Metal selectivity determinants in a family of transition metal transporters. *J. Biol. Chem.* **287,** 3185–3196 (2012).
20. Lin, H. *et al.* Gain-of-function mutations identify amino acids within transmembrane domains of the yeast vacuolar transporter Zrc1 that determine metal specificity. *Biochem. J.* **422,** 273–283 (2009).
21. Coudray, N. *et al.* Inward-facing conformation of the zinc transporter YiiP revealed by cryoelectron microscopy. *Proc. Natl Acad. Sci. USA* **110,** 2140–2145 (2013).
22. Hinds, B. J. *et al.* Aligned multiwalled carbon nanotube membranes. *Science* **303,** 62–65 (2004).
23. Hoch, E. *et al.* Histidine pairing at the metal transport site of mammalian ZnT transporters controls Zn2+ over Cd2+ selectivity. *Proc. Natl Acad. Sci. USA* **109,** 7202–7207 (2012).
24. Ramos, S., Schuldiner, S. & Kaback, H. R. The electrochemical gradient of protons and its relationship to active transport in *Escherichia coli* membrane vesicles. *Proc. Natl Acad. Sci. USA* **73,** 1892–1896 (1976).
25. Gupta, S., Sullivan, M., Toomey, J., Kiselar, J. & Chance, M. R. The Beamline X28C of the Center for Synchrotron Biosciences: a national resource for biomolecular structure and dynamics experiments using synchrotron footprinting. *J. Synchrotron Radiat.* **14,** 233–243 (2007).
26. Kaur, P., Kiselar, J. G. & Chance, M. R. Integrated algorithms for high-throughput examination of covalently labeled biomolecules by structural mass spectrometry. *Anal. Chem.* **81,** 8141–8149 (2009).
27. Ralston, C. Y. *et al.* Time-resolved synchrotron X-ray footprinting and its application to RNA folding. *Methods Enzymol.* **317,** 353–368 (2000).

Acknowledgements We dedicate this work to the memory of Peter C. Maloney, who read and commented on a version of the manuscript. This work was supported in part by the National Institutes of Health under grant R01 GM065137 (to D.F.), the Division of Chemical Sciences, Geosciences, and Biosciences, Office of Basic Energy Sciences of the US Department of Energy (DOE) under contract DE-AC02-98CH10886 (to D.F.); D.F. is primarily supported by the Physical Biosciences Program, Office of Basic Energy Sciences of the DOE and the National Institute for Biomedical Imaging and Bioengineering under grants P30-EB-09998 and R01-EB-09688 (to M.R.C.). The National Synchrotron Light Source at Brookhaven National Laboratory is supported by the DOE under contract DE-AC02-98CH10886.

Author Contributions M.R.C. and D.F. conceived the work, S.G. and D.F. designed the experiments, S.G., J.C., R.D. and D.F. performed the experiments, S.G., M.R.C. and D.F analysed the data, and D.F. interpreted the data and wrote the paper with S.G. and M.R.C.

Author Information Reprints and permissions information is available at www.nature.com/reprints. The authors declare no competing financial interests. Readers are welcome to comment on the online version of the paper. Correspondence and requests for materials should be addressed to D.F. (dfu3@jhmi.edu) or M.R.C. (mrc16@case.edu).

METHODS

Preparation of apo-YiiP and zinc-YiiP for X-ray radiolysis. His-tagged YiiP was overexpressed in BL21(DE3) pLysS cells and purified as described previously[3]. Briefly, cells in the stationary phase of an overnight auto-induction culture were harvested and lysed mechanically by three passages through a microfluidizer press cell. The resulting membrane vesicles were pelleted by ultracentrifugation, and then solubilized using a detergent buffer containing 100 mM NaCl, 20 mM HEPES, pH 7.5, 7% *n*-dodecyl-β-D-maltopyranoside, 0.25 mM Tris(2-carboxyethyl) phosphine hydrochloride (TECP) and 20% w/v glycerol. The crude membrane extract was applied to a Ni^{2+}-NTA superflow column. After washing the column with 20 mM HEPES, pH 7.5, 300 mM NaCl, 20% w/v glycerol, 0.05% DDM, 0.25 mM TCEP, 30 mM imidazole, YiiP was eluted with an elevated imidazole concentration at 500 mM. The purified His-YiiP was loaded to a 10 kDa cutoff dialysis cassette against a bulk solution containing 20 mM HEPES, pH 7.5, 100 mM NaCl, 20% w/v glycerol, 0.05% DDM, 0.25 mM TCEP. Thrombin (Novagen) was added into the dialysis cassette at a ratio of one unit per milligram of His-YiiP. The proteolytic removal of the His-tag was confirmed by matrix-assisted laser desorption/ionization time-of-flight mass spectrometry. Prior to X-ray exposure, YiiP was de-metallized by incubation with 5 mM EDTA for 30 min. The EDTA-treated sample was then subjected to size-exclusion purification using a TSK $3000SW_{XL}$ column pre-equilibrated with a radiolytic labelling buffer (10 mM NaPi, pH 6.5, 100 mM NaCl, 0.02% DDM, 0.1 mM TCEP). The purified YiiP is referred to as apo-YiiP hereafter. A total of 2.5 titratable zinc sites in each apo-YiiP monomer were detected by isothermal titration calorimetry[3]. These zinc sites were mapped to a transport site in the TMD, a surface zinc-binding site on the cytoplasmic membrane surface and a partly occupied binuclear zinc-binding site in the C-terminal CTD[13]. $ZnCl_2$ was added to 0.1 mM to an aliquot of apo-YiiP to form zinc-YiiP at 10 μM concentration. At this zinc concentration, the transport site in zinc-YiiP was mostly occupied because the zinc-binding affinity of the transport site was in the micromolar range[3].

Synchrotron X-ray radiolysis, mass spectrometry and data analysis. Apo-YiiP or zinc-YiiP were exposed to an X-ray white beam at beamline X28C of the National Synchrotron Light Source, Brookhaven National Laboratory, as described previously (Extended Data Fig. 1a)[16,25]. Briefly, X-ray beam parameters were optimized to provide a sufficient dose of hydroxyl radical in a millisecond timeframe as judged by a standard fluorophore assay[25]. A Kintek quench flow apparatus (KinTek Corporation) was modified to push 200 μl of protein samples through an X-ray window (0.8 mm internal diameter × 4 mm length) at various flow-speeds that gave an X-ray irradiation time ranging from 2.5 to 20 ms. All irradiations were performed at 4 °C. Unwanted secondary oxidations were quenched within 40 ms by collecting the irradiated samples directly in a tube containing 10 mM methionine amide, and then frozen at −80 °C. The 'zero' sample was run under the same condition without opening the beamline shutter. Proteolytic cleavage of the irradiated samples was performed using pepsin, trypsin or trypsin–chymotrypsin double digestion to obtain maximum sequence coverage. For pepsin digestion, the detergent in the samples was first removed by methanol–water–chloroform precipitation followed by pepsin digestion at 37 °C for 10 min. For trypsin and trypsin–chymotrypsin digestion, protein samples were incubated with the proteases overnight at 37 °C, followed by detergent removal using an affinity spin column (Thermo Scientific). A bottom-up proteomics analysis by reverse phase LC–MS was performed using a Dionex Ultimate 3000 RSLCnano LC interfaced to a Fourier Transform LTQ mass spectrometer (Thermo Scientific). The digests (~1 pmol) were loaded onto a PepMap reverse-phase trapping column (300 μm × 5 mm C18) to enrich the peptides and wash away excess salts using a nano-HPLC UltiMate-3000 column switching technique; reverse-phase separation was then performed on a C18, PepMap column (75 μm × 15 cm). Buffer A (100% water and 0.1% formic acid) and buffer B (20% water, 80% acetonitrile and 0.1% formic acid) were employed in a linear gradient. Proteolytic peptides eluted by an acetonitrile gradient (1% per min) were directed to an LTQ-FT mass spectrometer (Thermo Scientific) equipped with a nanospray ion source operated at a needle voltage of 2.4 kV. Mass spectra were acquired in the positive-ion mode with the following acquisition cycle: a full scan recorded in the Fourier transform analyser at resolution (*R*) 100,000 followed by MS/MS of the eight most intense peptide ions in a linear trap quadrupole analyser. The MS/MS data for peptides and their sites of modifications were manually interpreted with the aid of the ProteinProspector algorithm (University of California, San Francisco), ProtMap[26] and Bioworks 3.3 (Thermo Scientific). The peak area from the extracted ion chromatograms of a specific peptide fragment with a particular *m*/*z* ratio and associated +14, +16 or +32 Da side-chain modifications was used to quantify the amount of modification at a given irradiation time. The fraction of unmodification versus the X-ray irradiation time was plotted and fitted to a single exponential function using Origin 7.5 (OriginLabs) to determine the hydroxyl radical reactivity rate of the side chain[16]. All data are presented as mean ± s.e.m. based on three or more independent measurements.

Time-resolved synchrotron X-ray radiolysis. Time-resolved radiolysis was performed in a modified KinTek apparatus using a three-step (push–pause–push) flow sequence (Extended Data Fig. 1b)[18,27]. A 20 μl amount of 20 μM apo-YiiP in the radiolysis buffer and an equal volume of 0.2 mM $ZnCl_2$ in the radiolysis buffer were pushed into a T-mixer. After a designated delay time from 0 to 10 s, a second push drove the mixed sample through an irradiation cell and then into a collection tube containing methionine amide to a final concentration of 10 mM. The sample flow speed was calibrated to achieve 2.5 ms of fixed X-ray irradiation in the irradiation cell. The dead time for the sample to travel from the T-mixer to the irradiation cell was 10 ms. The reaction time was the sum of the dead time and the delay time for the sample to be held in the mixing loop. Mass spectrometric measurements of radiolytic labelling and data analysis followed the same procedure as described above. The extent of radiolytic modification was plotted against the reaction time and fitted with a single exponential function to determine the rate of water accessibility change to the site of radiolytic modification. All data are presented as mean ± s.e.m. based on three or more independent measurements.

Mutagenesis, mutant expression and stability assay. L152 mutations were generated using a Quick Change site-directed mutagenesis kit (Agilent Technologies). The L152 mutants were produced by auto-induction overexpression, DDM solubilization and Ni-NTA affinity purification as described above. The purified proteins were further purified by sizing HPLC using a TSK$3000SW_{XL}$ column equilibrated with 20 mM HEPES, pH 7.0, 100 mM NaCl, 12.5% glycerol, 0.05% DDM and 2 mM β-ME. Protein expression was examined before DDM solubilization. Membrane vesicles were directly solubilized by SDS and then subjected to western blot detection using rabbit affinity-purified His-tag polyclonal antibody (catalogue number 2365) purchased from Cell Signaling Technology. Western blots were performed three times. Protein stability was monitored by size-exclusion HPLC. Equal amounts of purified L152 mutants and YiiP were kept in the HPLC buffer for 24 h at 4 °C, then protein aggregates were removed by ultracentrifugation. The resultant supernatants were injected to the TSK column. The eluted peaks were recoded using the wild-type YiiP peak as a reference.

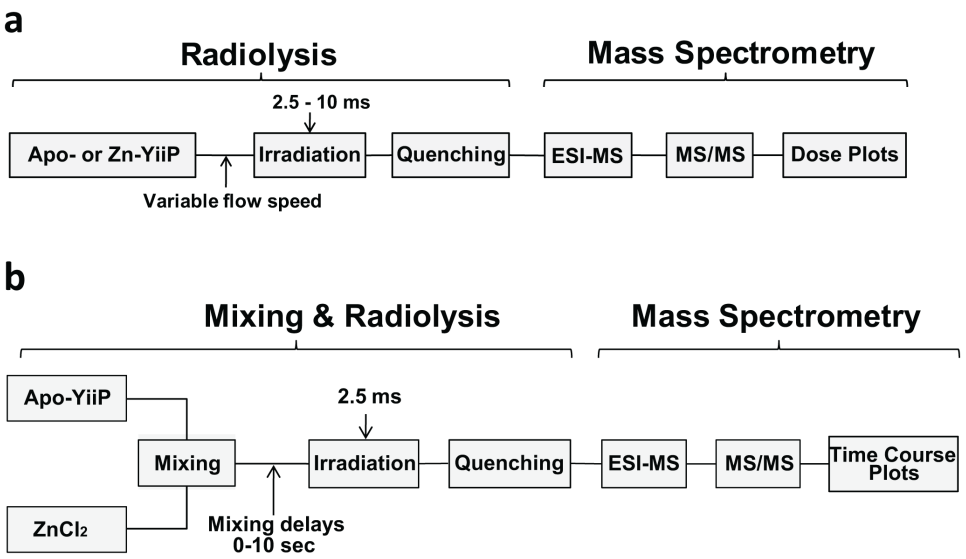

Extended Data Figure 1 | Steady state and time-resolved synchrotron X-ray radiolysis. **a**, Experimental scheme for obtaining steady state dose plots. **b**, Experimental schemes for obtaining the time course of water accessibility change.

a

TM1 TM2

1MNQSYGRLVS11RAAIAATAMA21SLLLLIKIFA31WWYTGSVSIL41AALVDSLVDI51

TM3

GASLTNLLVV61RYSLQPADDN71HSFGHGKAES81LAALAQSMFI91SGSALFLFLT

TM4 TM5

101GIQHLISPTP111MTDPGVGVIV121TIVALICTII131LVSFQRWVVR141RTQSQAVR

TM6

AD151MLHYQSDVMM161NGAILLALGL171SWYGWHRADA181LFALGIGIYI191LYSAL

RMGYE201AVQSLLDRAL211PDEERQEIID221IVTSWPGVSG231AHDLRTRQSG241P

TRFIQIHLE251MEDSLPLVQA261HMVADQVEQA271ILRRFPGSDV281IIHQDPCSVV

291PIHLVPR

b

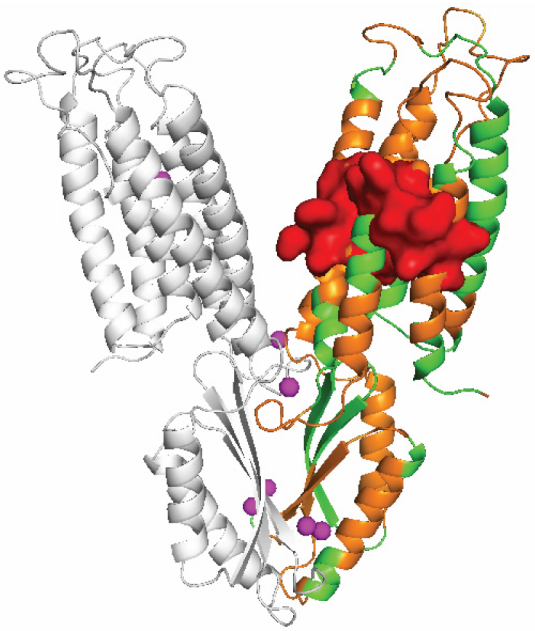

Extended Data Figure 2 | Proteomics sequence coverage of YiiP. **a**, Mass spectrometry sequence coverage. The detectable peptides, undetectable residues and coordination residues of the transport site are shown in orange, green and red, respectively. Transmembrane helixes (TMs) are underlined as indicated. **b**, Mapping detectable proteolytic peptides to the YiiP crystal structure. Detectable and undetectable peptides in one protomer of a YiiP homodimer are coloured in orange and green, respectively. The side chains of detectable residues located between two cavities are shown in surface representation and coloured in red. Bound zinc ions are shown as magenta spheres.

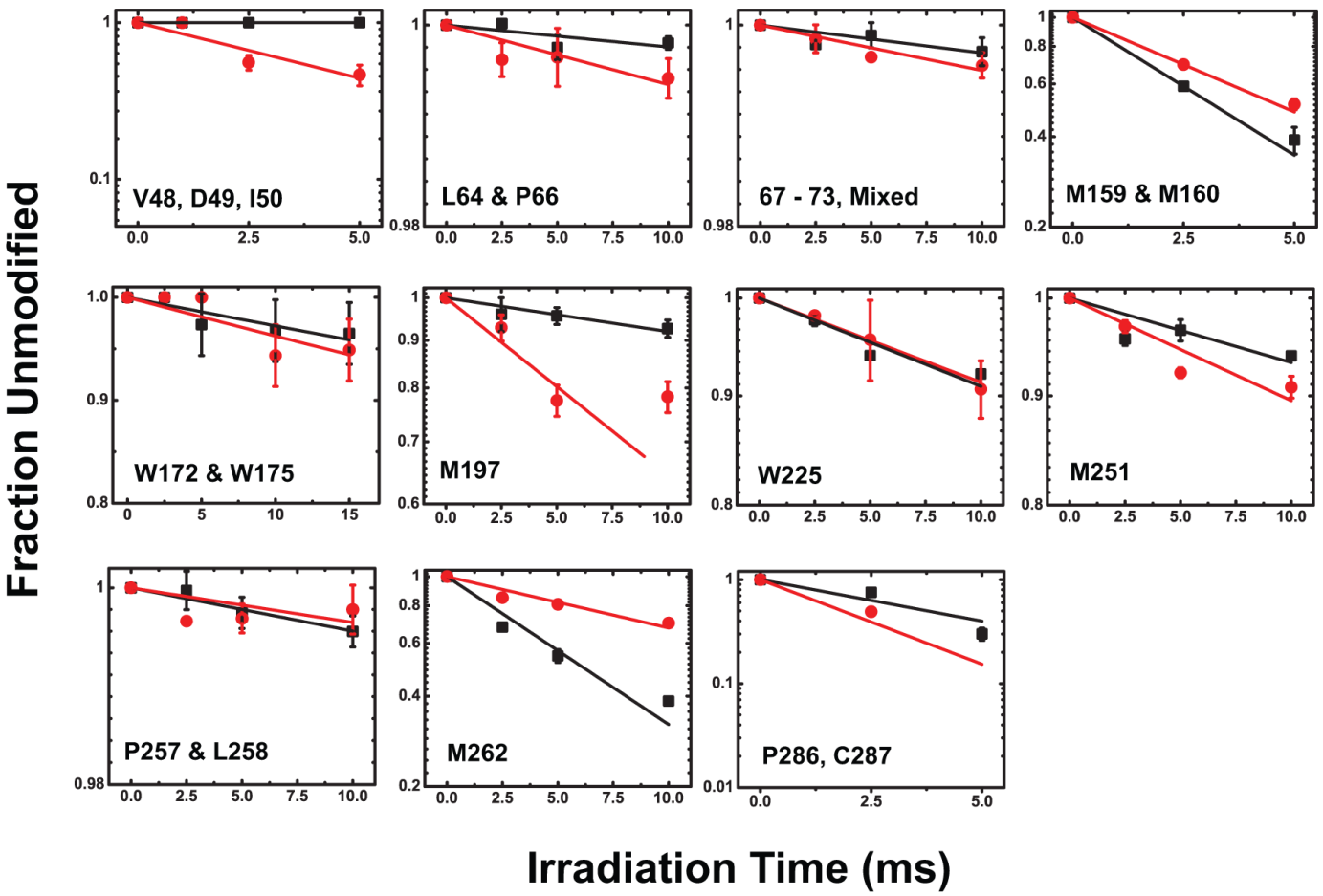

Extended Data Figure 3 | Dose–responses for modified sites in apo-YiiP (red) and zinc-YiiP (black). Solid lines represent least-squares fits of the means of the dose-dependent data as described in Methods. The reactivity rate for each site as indicated is summarized in Extended Data Table 1. Note, the linear dose–response on a logarithm scale indicates negligible radiation damage by 10 ms irradiation to all sites except M151, M197 and P286C287, which reached saturation at 5 ms. In these cases, the 10 ms data points were not used in linear regression. Dose–response plots for M151 and L152 are shown in Fig. 1d. Zinc binding to a solvent-exposed zinc site located on the cytoplasmic membrane surface (Z2, Fig. 2b) yielded 38–67% reductions in oxidative modification of neighbouring L64, P66, D68, D69, H71 and F73 within the peptide SLQPADDNHSF (Extended Data Table 1). A marginal 20% reduction in water accessibility change by zinc binding was also localized to W172 and W175 within an extracellular loop connecting TM5 and TM6 (Fig. 2b). This loop is disordered in the crystal structure. Structural flexibility probably allows for distinct loop conformations in response to zinc binding. A total of six modified sites were identified in CTD (Extended Data Table 1). Two sites (M251 and P286/C287) with reduced water accessibility for zinc-YiiP are located near the binuclear zinc-binding site at the CDT–CDT interface. Zinc binding may partly protect these sites from labelling, but the protection was incomplete because of the solvent exposure. Two sites on the CTD protein surface (W225 and P257/L258) showed no detectable change as expected for fully exposed residues. Still two more sites exhibited an increase in water accessibility for zinc-YiiP. The first site (D207–L210) was detected with low signal-to-noise ratio and mapped to a TMD-CDT linker, which is involved in a hinge-like conformational change in response to zinc binding[1]. The second site involved M262 on the CDT surface. There was no obvious explanation for the increase of water accessibility to this methionine residue.

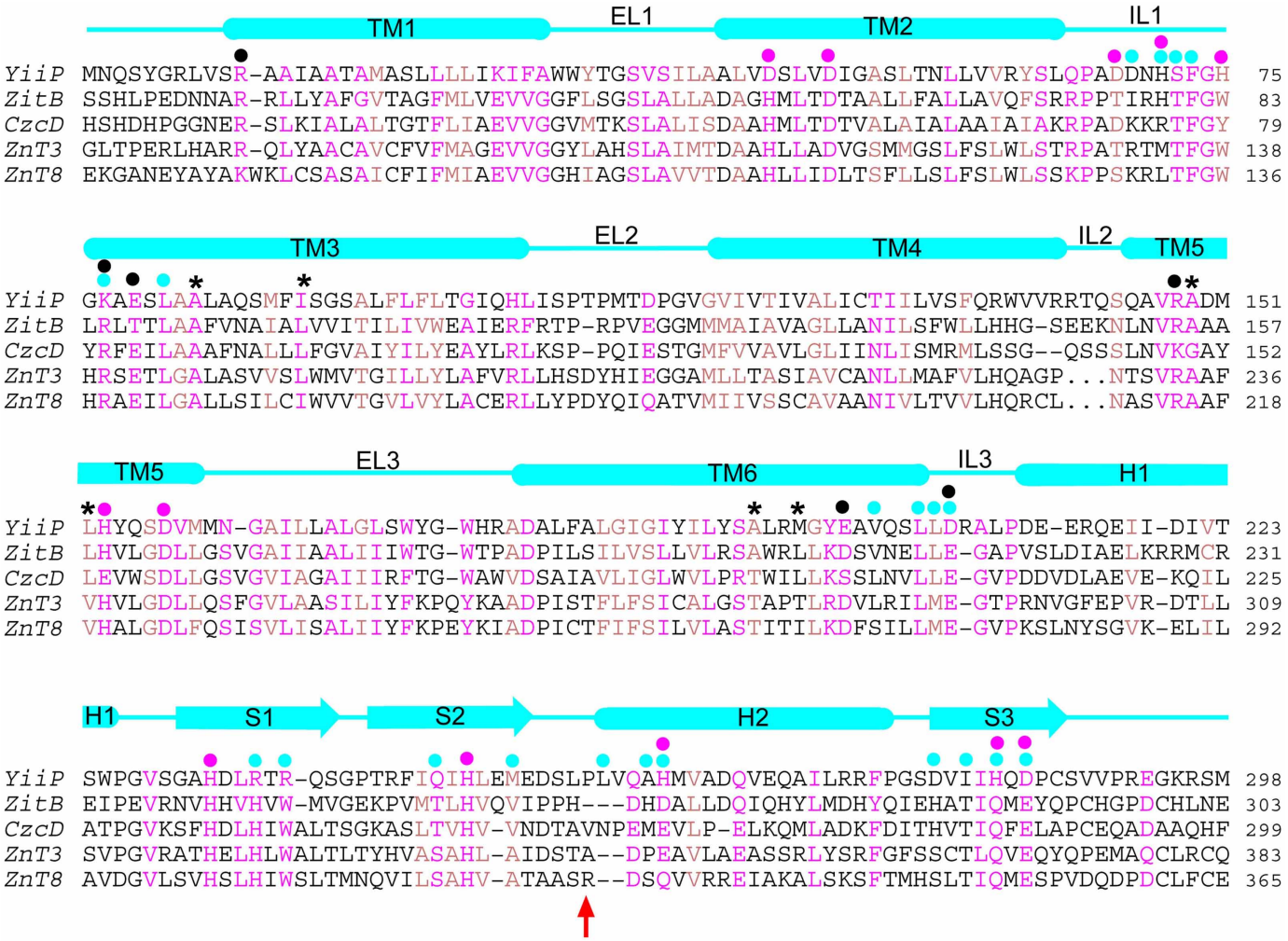

Extended Data Figure 4 | Sequence conservation of the inter-cavity seal. Residues involved in TM5→TM3–TM6 packing are marked by black asterisks in a CDF sequence alignment. Conserved and homologous residues are coloured in magenta and light brown. Magenta, cyan and black dots indicate residues involved in zinc coordination, dimerization contacts and the interlocked (Lys 77–Asp 207)$_2$ salt-bridges, respectively. Dashed lines in two human ZnT sequences represent omitted residues in a loop (IL2) between TM4 and TM5. The red arrow indicates the position of the R325W mutation in human ZnT8.

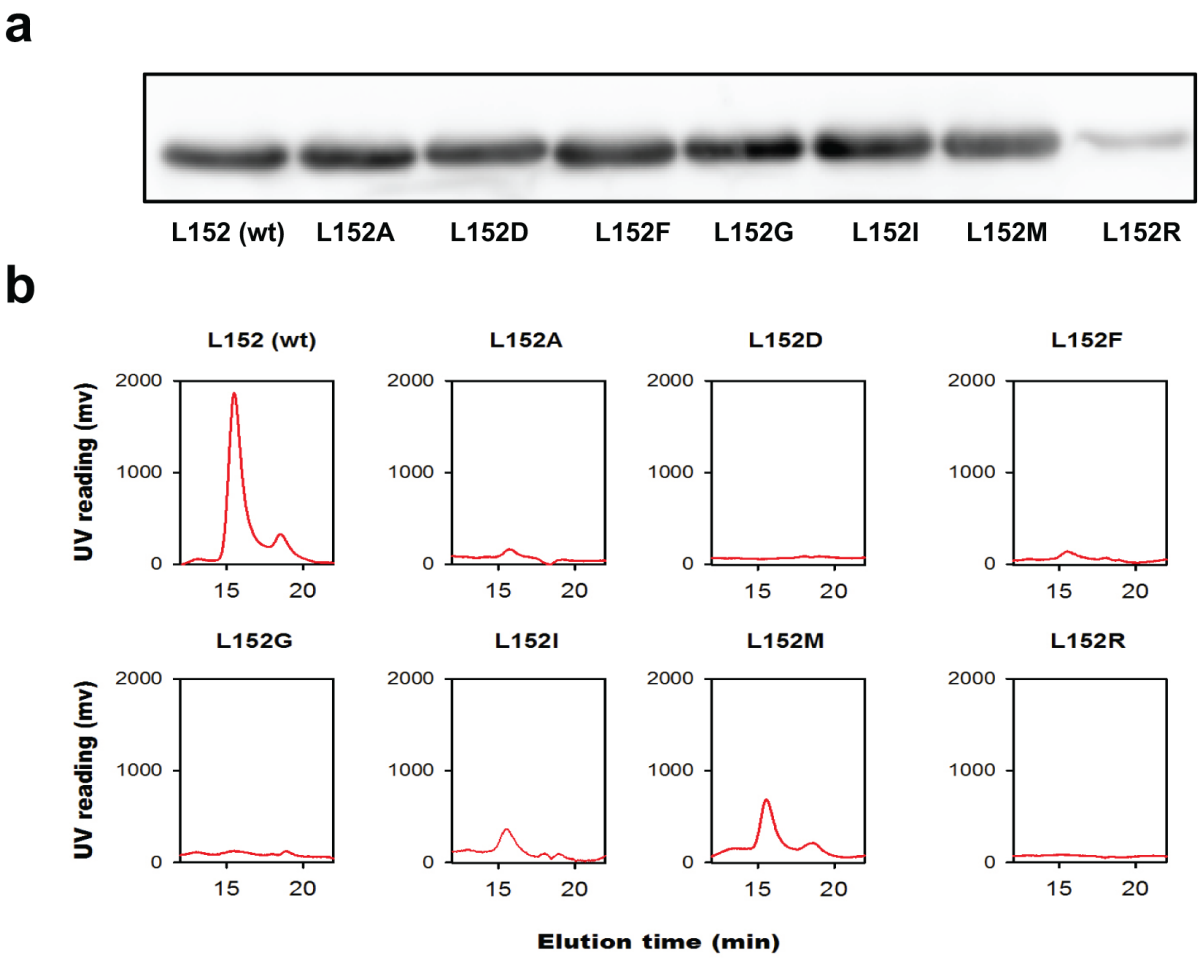

Extended Data Figure 5 | Expression and size-exclusion analysis of purified L152 mutants. L152 was substituted by an A, D, F, G, I, M or R residue to evaluate the effect of L152 mutations on structural stability. **a**, Western blot analysis of the expression of YiiP and L152 mutants as indicated. Only a L152R point mutation caused a modest reduction of protein expression, whereas other L152 substitutions and wild-type YiiP showed a similar level of expression based on western blot detection of His-tagged proteins in membrane vesicles using a monoclonal antibody against the poly-histidine tag. **b**, Eluted protein peaks for YiiP and L152 mutants as indicated after the removal of protein aggregates by ultracentrifugation. YiiP and L152 mutants were solubilized by DDM and purified by Ni-NTA affinity chromatography and size-exclusion HPLC. The purified wild-type YiiP remained stable in DDM micelles for weeks. Sizing HPLC analysis showed a monodisperse YiiP peak followed by a minor detergent peak eluted at expected retention times[6]. In sharp contrast, purified L152 mutants rapidly denatured, forming lager protein aggregates. After removing the aggregates by ultracentrifugation, none of the purified L152A, D, F, G and R became detectable by sizing HPLC. Two conserved L152 substitutions, L152I and L152M, showed a significantly reduced peak volume within 48 h of DDM solubilization. A prolonged DDM solubilization led to complete denaturation of L152I and L152M while the wild-type YiiP remained stable under the same experimental conditions. Thus, L152 is critically important to the protein stability in detergent micelles. The lack of protein stability in detergent solution precluded functional reconstitution and characterization of purified L152 mutants.

Extended Data Table 1 | Summary of the sites of radiolytic labelling and their reactivity rates for zinc-YiiP and apo-YiiP

Seq No.*	Sequence †	Modified residues and observed mass shifts ‡	k s^{-1} Zinc-YiiP§	k s^{-1} Apo-YiiP§	Ratio (R)‖
5-8	YGRL	-¶	-	-	-
15-27	AATAMASLLLLIK	-	-	-	-
32-40	WYTGSVSIL	-	-	-	-
41-47	AALVDSL	-	-	-	-
47-50	LVDI	**V48,D49,I50** (+14 Da)	0.05± 0.1	163.0 ± 25	$3 \times 10^{-4} \pm 4 \times 10^{-5}$
58-62	LLVVRY	-	-	-	-
63-73	SLQPADDNHSF	**L64,P66** (+16 Da)	0.2 ± 0.1	0.6 ± 0.1	0.37 ±0.2
		D68,D69,H71,F73 (+16 Da)	0.3 ± 0.06	0.5 ± 0.06	0.62 ± 0.2
82-88	AALAQSM	-	-	-	-
82-89	AALAQSMF	-	-	-	-
90-96	ISGSALF	-	-	-	-
97-101	LFLTG	-	-	-	-
106-111	ISPTPM	-	-	-	-
137-140	WVVR	-	-	-	-
149-154	ADMLHY	**M151** (+16 Da)	35.5 ± 6.0	14.4 ± 2.4	2.5 ± 0.8
		L152 (+14 Da)	0.05 ± 0.1	8.5 ± 0.7	0.006 ± 0.002
149-177	ADMLHYQSDVMM NGAILLALGLSWYGWHR#	**W172, W175** (+32 Da)	2.8 ± 0.6	3.8 ± 0.6	0.8 ± 0.3
158-165	VMMNGAIL	**M159,M160** (+16 Da)	213 ± 1.0	142 ± 0.5	1.5 ± 0.01
178-196	ADALFALGIGIYILYSALR	-	-	-	-
185-189	GIGIY	-	-	-	-
197-208	MGYEAVQSLLDR	**M197** (+16 Da)	8.3 ± 3.0	30.8 ± 4.4	0.3 ± 0.1
207-220	DRALPDEERQEIIDLL*	**207-210** (+ 16)	6.0 ± 2.0	5.0 ± 2.0	1.6 ±1.0
209-225	ALPDEERQEIIDIVTSW	**W225** (+32 Da)	9.1 ± 0.7	9.5 ± 0.8	0.97 ± 0.2
247-258	IHLEMEDSLPL	**M251** (+ 16 Da)	6.9 ± 1.4	11.1 ± 1.5	0.65 ± 2
		P257,L258 (+ 14 Da)	0.4 ± 0.1	0.4 ± 0.1	1 ± 0.5
262-272	MVADQVEQAIL	**M262** (+ 16 Da)	113.5 ± 10	39.4 ± 5.5	3 ± 0.7
275-283	FPGSDVIIH	-	-	-	-
275-287	RFPGSDVIIHQDPC	**P286,C287** (+ 16 Da)	184 ± 44	374 ± 80	0.54 ± 0.23

* More than 80% sequence coverage was obtained from the bottom-up LC–electro-spray ionization–MS analysis of YiiP using pepsin, trypsin and trypsin–chymotrypsin digestions.
† Sequences of digested fragments identified by mass spectrometry analysis described in methods.
‡ Positions of modified residues identified by mass spectrometry analysis described in Methods. Where multiple residues are indicated, the rate is a sum of the results from the indicated residues.
§ Rate constants were estimated by employing a nonlinear fit of hydroxyl radical modification data to a first-order decay as described in Methods.
‖ Ratio (*R*) of hydroxyl radical reactivity rate between zinc-YiiP and apo-YiiP from four to six independent measurements. *R* is a quantitative measure of the change in the solvent accessibility from apo-YiiP to zinc-YiiP.
¶ No modification was detected.
# Modification of +16 Da was observed at the multiple Met residues in accordance with the observation of peptide 149–154 and 158–165. Here we report only the modification at W172 and W175 that showed distinctive +32 Da modification.
★ Modification of +16 Da was detected at 209 and 210 in accordance with the observation of peptide 207–220. The rate constants on these residues are obtained from other peptides shown in the table. Here we report only the modification at W225 that showed distinctive +32 Da modification.